Neutron capture cross section of ^{241}Am

M. Jandel,[1,*] T. A. Bredeweg,[1] E. M. Bond,[1] M. B. Chadwick,[1] R. R. Clement,[1] A. Couture,[1] J. M. O'Donnell,[1] R. C. Haight,[1] T. Kawano,[1] R. Reifarth,[1,†] R. S. Rundberg,[1] J. L. Ullmann,[1] D. J. Vieira,[1] J. B. Wilhelmy,[1] J. M. Wouters,[1] U. Agvaanluvsan,[2] W. E. Parker,[2] C. Y. Wu,[2] and J. A. Becker[2]

[1]*Los Alamos National Laboratory, Los Alamos, New Mexico 87545, USA*

[2]*Lawrence Livermore National Laboratory, Livermore, California 94550, USA*

(Received 27 May 2008; published 24 September 2008; corrected 30 September 2008)

The neutron capture cross section of ^{241}Am for incident neutrons from 0.02 eV to 320 keV has been measured with the detector for advanced neutron capture experiments (DANCE) at the Los Alamos Neutron Science Center. The thermal neutron capture cross section was determined to be 665 ± 33 b. Our result is in good agreement with other recent measurements. Resonance parameters for $E_n < 12$ eV were obtained using an R-matrix fit to the measured cross section. The results are compared with values from the ENDF/B-VII.0, Mughabghab, JENDL-3.3, and JEFF-3.1 evaluations. Γ_n neutron widths for the first three resonances are systematically larger by 5–15% than the ENDF/B-VII.0 values. The resonance integral above 0.5 eV was determined to be 1553±7 b. Cross sections in the resolved and unresolved energy regions above 12 eV were calculated using the Hauser-Feshbach theory incorporating the width-fluctuation correction of Moldauer. The calculated results agree well with the measured data, and the extracted averaged resonance parameters in the unresolved resonance region are consistent with those for the resolved resonances.

DOI: 10.1103/PhysRevC.78.034609 PACS number(s): 25.40.Lw, 25.40.Ny, 28.20.Ka, 27.90.+b

I. INTRODUCTION

New reactor concepts have boosted interest in improved cross section data for neutron-induced reactions on major and minor actinides. ^{241}Am is always present in Pu-containing nuclear fuels because of the β-decay of ^{241}Pu ($t_{1/2} = 14.4$ yr) and the complex network of reactions that take place in high neutron fluence environments (see Fig. 1). Therefore, accurate cross section data are critical in the development of new advanced fast reactors as they are envisioned in the Global Nuclear Energy Partnership (GNEP) [1] and in the transmutation of nuclear waste. Cross section information is also important for an improved interpretation of radiochemical diagnostics, such as the ^{242}Cm/^{241}Am ratio, which are relevant to the U.S. Department of Energy's Stockpile Stewardship Program and the threat reduction/nuclear forensics arena. Improved ^{241}Am(n,γ) cross section data that lead to the production of ^{242}Am and its subsequent β decay to ^{242}Cm provides important quantitative information about nuclear device performance and nuclear forensics characterization of a terrorist nuclear event.

An extensive set of experimental data has been reported on the ^{241}Am(n,γ) reaction [2–15]. Many of these measurements were performed more than 30 years ago using C_6D_6 detectors for spectroscopy. Scattered neutron background subtraction is a concern with these measurements. At present there is poor agreement on the thermal capture cross section. Data evaluations for several low-energy neutron resonances disagree significantly, especially for the first few resonances (see Sec. IV B). The cross sections in the 1–10 keV energy region have 5–15% differences between the various data evaluations, and measurements at higher energies (>200 keV) deviate at the 50% level. We have undertaken new measurements using the latest technology and experimental equipment to reduce the ^{241}Am(n,γ) cross section uncertainties. The state-of-the-art detector for advanced neutron capture experiments (DANCE) at Los Alamos National Laboratory was designed and built to enable this and other similar neutron capture measurements [16].

We report the radiative neutron capture cross section on ^{241}Am for incident neutron energies between 0.02 eV and 320 keV. Methods of total γ-ray calorimetry were used to identify capture events on an event-by-event basis using information on γ-ray multiplicity and total γ-ray energy. The neutron capture process populates either the 16-h ground state ^{242g}Am or the 141-yr ^{242m}Am isomer. Since DANCE does not have sufficient total γ-ray energy resolution to intrinsically resolve events leading to the isomer ($E^* = 49$ keV) from the ground state, the results shown here represent the total neutron capture cross section leading to both the isomer and ground state, as a function of neutron energy. Fission contributions in both the resonance and continuum regions are predicted to be at most 1% of capture. After data reduction and analysis, the fission contribution is negligible and therefore no corrections were needed.

II. EXPERIMENT

A. DANCE

DANCE is located on the 20.2-m neutron flight path 14 of the Manuel Lujan Jr. Neutron Scattering Center at the Los Alamos Neutron Science Center (LANSCE) [17]. DANCE consists of 160 BaF_2 crystals arranged in a 4π geometry. Each crystal has a depth of 15 cm and a volume of ∼734 cm^3.

*mjandel@lanl.gov

†Present affiliation: Gesellschaft für Schwerionenforschung mbH, Darmstadt, D-64291, Germany.

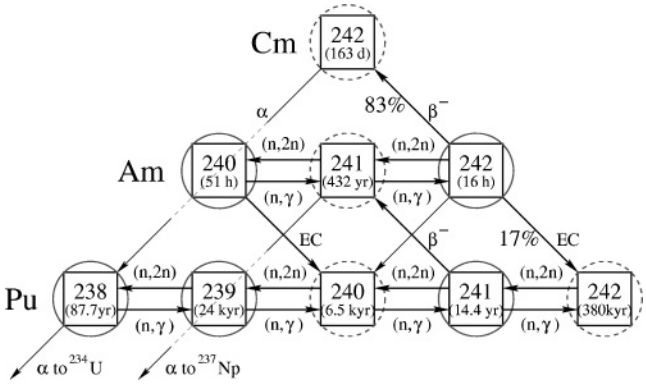

FIG. 1. Production/destruction network of nuclear reactions in plutonium-containing nuclear fuel leading to the formation of americium and curium isotopes.

The high photopeak efficiency of the BaF_2 crystals, the segmentation, and the large solid angle coverage enable DANCE to measure prompt γ rays following neutron capture on small samples, isotopically enriched or radioactive, that are on the order of hundreds of $\mu g/cm^2$. The DANCE array efficiency for detecting a single 1-MeV γ ray is approximately 86% [18], and for a typical γ-ray cascade that follows neutron capture, where 3–4γ rays are emitted, the total efficiency is above 95%. Another advantage of the BaF_2 scintillator is its fast timing which leads to a good γ-γ coincidence timing and a precise determination of the neutron time-of-flight.

A ^{6}LiH shell of 6-cm thickness surrounds the target and reduces the number of target scattered neutrons from reacting in the BaF_2 crystals, causing an unwanted background. The isotopic composition of Li in the ^{6}LiH shell is 86% ^{6}Li and 14% ^{7}Li, and the density of the ^{6}LiH shell is 0.7288 g/cm^3. Scattered neutrons are attenuated due to the ^{6}Li(n,α) reaction. Transmitted neutrons can induce (n,γ) reactions in the BaF_2 crystals either promptly or during the slowing down process. Such background events detected by DANCE are removed from the data in the off-line analysis.

A background component originating from the natural α decay of Ra inherently present in the crystals is removed from the data analysis by using differences in the emission spectrum of BaF_2 as described below. The emission spectrum has two components: a fast component with a 220-nm wavelength and 0.6-ns decay time constant, and a slow component with a 310-nm wavelength and 600-ns decay time constant [19,20]. The amplitudes of the two components of the scintillation light output are a function of energy, mass, and charge of the interacting particle. The characteristic ratio of fast-to-slow component light output in the BaF_2 pulse was used to discriminate α particles from γ rays. The fast component was obtained by integrating the BaF_2 signal during the first 64 ns, and the slow component was obtained by integrating the signal in the next 1 μs [21].

The BaF_2 crystals were calibrated using ^{88}Y, ^{22}Na, and ^{60}Co γ-ray standards. Small gain shifts were observed in the light output of each crystal and corrections were applied to stabilize these energy shifts taking advantage of the Ra α-decay energy measured in each BaF_2 crystal during the course of the experiment. The positions of the α peaks were fitted for each crystal and for each run.

Time delays of signals from the crystals were found to deviate also. The deviations were corrected for each run using the average time difference between the γ-ray events in the crystal and the reference crystal. The reference crystal was chosen in the beginning of the data analysis.

B. Data Acquisition of DANCE

A detailed description of the DANCE data acquisition (DAQ) may be found in Ref. [21]. Herein we briefly summarize the acquisition settings for this experiment.

The photomultiplier output signal from each BaF_2 crystal was digitized in an Acqiris DC265 digitizer with 8-bit resolution at a sampling rate of 500 MHz (i.e., 2-ns sampling interval). Because of the high data rates involved (typically 10 kHz per crystal $\times$ 160 crystals), each wave form was processed online to obtain the following information before writing data to disk: (1) the presample integral of a background baseline reduced to one integral of 100-ns width, (2) the fast component of the light output(32 data points at 2-ns sampling), (3) the slow component reduced to five sequential integrals each 200 ns wide, and (4) two time stamps, relative to the beam pulse and a master clock. The data from the 15 front-end computers were correlated by a single rack-mounted computer and written to a MIDAS data structure [22].

The DANCE DAQ was configured in two different data acquisition modes, segmented and continuous, with different settings to cover the 7-decade incident neutron energy range from 20 meV up to 500 keV.

The segmented mode was used to cover the thermal to 50-eV energy region. Here, the DAQ was enabled with the proton beam pick-off trigger T_0, which arrives slightly before the beam pulse. An individual event was triggered when at least two crystals inside a γ-γ coincidence window of 200 ns registered a pulse above a 30-mV discriminator threshold, corresponding to a $\sim$120 keV γ energy. After a valid trigger, further data acquisition was blocked for 3.5 μs to allow for the event analysis and rearming of the Acqiris cards. The DAQ was stopped after a maximum "looking time" T_S, and the data were written to disk. Two different settings of T_S were used in this measurement: 14 and 2 ms, which cover the neutron energies of 0.02 eV to 0.5 MeV and 1.0 eV to 0.5 MeV, respectively. Although this covers the energy range of interest, the dead-time corrections inherent in this data acquisition mode become increasingly larger at neutron energies above 36 eV.

Therefore, for $E_n > 36$ eV, a second data acquisition mode, the so-called continuous mode, was used. Here, the DAQ system records data from all crystals in two independent 250-μs-wide windows starting from $T_0 + T_{\text{delay}}$. This mode is achieved by splitting the signal from each crystal and feeding them into two independent Acqiris digitizers. The delay times T_{delay} are then set to collect data in two different 250-μs-wide time-of-flight intervals. The entire wave form for each crystal is read out and processed as outlined above. For $T_{\text{delay}}(1) = 0$

and $T_{\rm delay}(2) = 250$ μs delay times, used in this measurement, we covered the neutron energy range from 6 eV to 0.5 MeV.

Off-line data analysis of the raw DANCE data was conducted as follows. The γ-γ hardware coincidence window of 100 ns was reduced to 20 ns. Signals due to α decay were removed from the data using a fast-slow component analysis, and the γ-ray data were calibrated using the run-by-run gain correction calibration files as mentioned in Sec. II A. An event was defined by the crystal γ-ray multiplicity (i.e., how many crystals fired), the corresponding γ-ray energy measured in each crystal, and the time when the event was registered. More precisely, the time of the event was defined by the first γ ray detected in a 20-ns coincidence window. Since the γ-ray photopeak efficiency was not 100%, Compton-scattered γ rays could either exit the DANCE array or be detected by other crystals. There was a large probability that the Compton-scattered γ ray from one crystal would be detected by one of its nearest neighboring crystals. Such an event would register as a multiplicity 2 event instead of multiplicity 1. To account for the Compton scattering, we performed the following "clusterization" procedure to obtain a closer representation of the true cascade γ-ray multiplicity. If the signal was detected in a crystal and no other signals were found in its neighboring crystals, then the cluster multiplicity 1 with crystal multiplicity 1 was registered. Signals from n neighboring crystals would be counted as cluster multiplicity 1 with crystal multiplicity $n+1$. The cluster multiplicity describes the true γ-ray cascade multiplicity better than the crystal multiplicity [18]. Therefore, from this point on, we will refer to the cluster γ-ray multiplicity for an event as simply the γ-ray multiplicity M_γ.

We also define a total γ-ray energy, $E_\gamma^{\rm total} = \sum_i E_{\gamma i}^{\rm single}$, where index i runs through the cluster multiplicity, $E_{\gamma i}^{\rm single}$ are the individual cluster γ-ray energies, and $E_\gamma^{\rm total}$ represents the total γ-ray energy detected in a single DANCE event. $E_\gamma^{\rm total}$ is equal to the Q value for the capture event if all cascade γ rays are detected.

C. ^{241}Am target

The ^{241}Am targets were prepared by the Nuclear and Radiochemistry Group at Los Alamos National Laboratory. The target material was electroplated onto two separate $\sim$2.5-μm-thick titanium backing foils. These two foils were mounted back-to-back with the ^{241}Am deposits on the outside. Thin aluminized Mylar foils (300-μg/cm^2 areal thickness) were used to cover the Am deposit to contain the spread of α-recoil daughter products. The diameter of the ^{241}Am deposit was 6.35 mm. The target was glued onto a thin G-10 frame and placed inside the target holder. The target holder had two 76-μm-thick Kapton windows for secondary target containment. The target holder was then installed inside the beampipe of the flight path and positioned at the center of the DANCE array.

The total mass of ^{241}Am was determined to be 219(1) μg by low-geometry α counting. The activity of the sample was $\sim$28 MBq and dominated by 59.5-keV γ emission following α decay. These γ rays did not affect the measurement, as they are strongly attenuated by the target holder, beampipe, and ^{6}LiH shell.

Neutron capture on ^{241}Am is followed by a γ-ray cascade leading to the ground state of ^{242}Am or the isomer ^{242m}Am. The total energy released in the cascade is equal to the Q value of the reaction 5.54 MeV plus the energy in the center of the mass of the incident neutron. As mentioned earlier, the feeding to the metastable ^{242m}Am state with the energy of 49 keV cannot be resolved by the DANCE array. The cross section derived here is thus the sum of the ^{241}Am(n,γ) cross sections to the ground state and the isomer.

III. EXPERIMENTAL DATA ANALYSIS

The (n,γ) cross section at a particular neutron energy E_n was determined from the following equation:

$$\sigma(n,\gamma)(E_n) = \frac{M}{N_A \rho_s} \frac{N_{n,\gamma}(E_n)}{\varepsilon_{n,\gamma}(E_n)\Phi(E_n)S}, \tag{1}$$

where N_A is the Avogadro's number, M is the molar mass, ρ_s is the areal density of the target, $N_{n,\gamma}$ is the number of measured capture events per eV per second, $\Phi(E_n)$ is the neutron flux, S is the illuminated target area, and $\varepsilon_{n,\gamma}$ is the total efficiency for detecting capture γ rays after applying gates on the event multiplicity and the total γ-ray energy set around the Q value of the (n,γ) reaction.

The following quantities are needed to deduce an accurate cross section at a particular neutron energy:

(i) Number of neutron capture cascades $N_{n,\gamma}$ after the background has been subtracted
(ii) Total efficiency of detecting the γ-ray cascade $\varepsilon_{n,\gamma}$ after applying the cuts on experimental data, namely, γ-ray multiplicity and total γ-ray sum energy
(iii) Neutron flux Φ at the target position
(iv) Mass of the target material.

The total cross section uncertainty $\Delta(\sigma(n,\gamma))$ is given by the standard uncertainty propagation formula

$$\Delta(\sigma(n,\gamma)) = \sqrt{\sum_{i=1}^{n} \left(\frac{\partial\sigma(n,\gamma)}{\partial V_i}\right)^2 \Delta V_i^2}, \tag{2}$$

where V_i represents ρ_s, Φ, $\varepsilon_{n,\gamma}$, and $N_{n,\gamma}$.

A. The yield of neutron capture cascade $N_{n,\gamma}$

Sorting and identification of γ rays that follow neutron capture relies on the calorimetric information that is acquired as a function of neutron energy. For each neutron energy bin, the information on γ-ray multiplicity and γ-ray energy is scrutinized in detail to distinguish the neutron capture γ rays from the γ-ray background. Figure 2 shows the measured counting rate as a function of of incident neutron energy for ^{241}Am. The measured raw data spectrum (solid line) is compared with the spectra obtained when different gates are applied on the γ-ray multiplicity and total γ-ray energy. A dotted line shows the spectrum gated on the cluster multiplicity

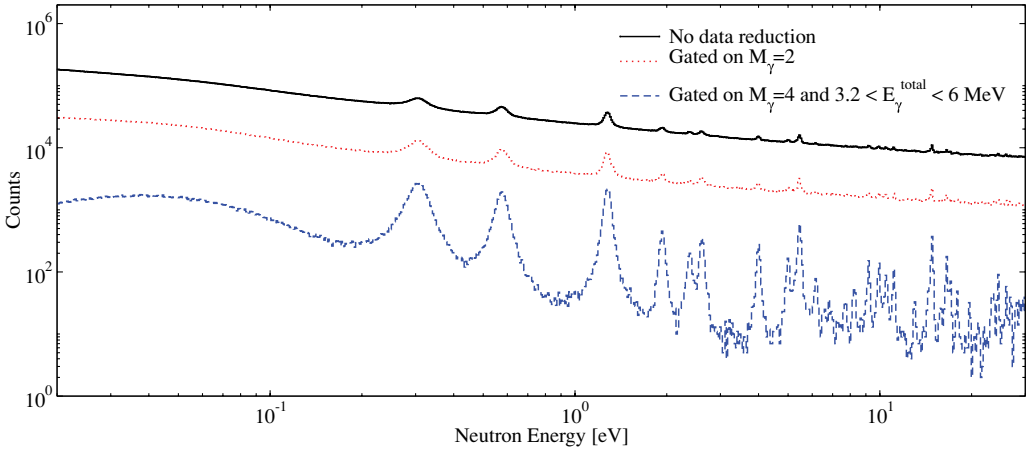

FIG. 2. (Color online) Experimental neutron capture spectra from DANCE taken with ^{241}Am target. The solid line shows the raw neutron capture spectrum obtained without any data reduction. The dotted line represents the neutron capture spectrum obtained for the γ-ray multiplicity events $M_\gamma = 2$. The dashed line shows the neutron capture spectrum obtained for events gated on γ-ray event multiplicity $M_\gamma = 4$ and total γ-ray energy between $3.2 < E_\gamma^{\text{total}} < 6$ MeV.

$M_\gamma = 2$, and a dashed line shows the spectrum gated on $M_\gamma = 4$ and $3.2 < E_\gamma^{\text{total}} < 6$ MeV. A noticeable increase in signal-to-noise is observed when the gates were applied making the resonances rise up from the background in the spectrum. The goal of the analysis was to find the conditions under which the signal-to-noise was optimized to extract the best results from the data.

The background was composed of several components. Constant cosmic-ray and varying accelerator backgrounds were present all the time during the measurement. β-decay events coming from the Ra decay chain, such as ^{214,210}Bi, were also present in the background. However, these background components induce events in the DANCE array that have low multiplicities and are independent of the incident neutron energy.

The backgrounds that depend on the neutron beam are more important. Background levels of γ rays are significantly different when the beam enters the DANCE experimental room, and the background has a strong neutron energy dependence. The most significant background component in this experiment was caused by neutrons scattered from the target holder components, the target backing, and the target itself. Some neutrons are scattered into the BaF_2 crystals despite the absorbing effects of the ^{6}LiH shell. Scattered neutrons slow down in the crystals and produce a neutron capture reaction followed by the emission of a γ-ray cascade. The Q values of radiative capture on Ba isotopes present in BaF_2 crystals are ^{135}Ba(n,γ) with $Q = 9.108$ MeV (natural abundance 6.6%), ^{137}Ba(n,γ) with $Q = 8.612$ MeV (n.a. 11.2%), ^{136}Ba(n,γ) with $Q = 6.906$ MeV (n.a. 7.9%), and ^{138}Ba(n,γ) with $Q = 4.723$ MeV (n.a. 71.7%).

Figure 3 shows total γ-ray energy spectra for different γ-ray multiplicities. The pronounced peak at 5.0 MeV observed in total γ-ray energy spectra corresponds to (n,γ) capture events on ^{241}Am. The Q value of ^{241}Am(n,γ) for this reaction is 5.54 MeV. The shift observed in the position of the peak is caused mainly by loss of low-energy γ rays due to the energy thresholds of each crystal, absorption of the low-energy γ rays by the ^{6}LiH shell, internal conversion, and Compton-scattered events exiting the DANCE array. It also includes inaccuracies in energy calibrations of the crystals. Despite the shift, the ^{241}Am capture peak is clearly identified using the γ-ray spectra for multiplicities with $M_\gamma > 2$. The peaks above the ^{241}Am(n,γ) reaction Q value correspond to the capture events on Ba isotopes in BaF_2 crystals.

To extract the yield of the ^{241}Am cascade, one has to properly subtract the background. The total γ-ray energy spectra of the background were measured using blank targets. The blank target consists of the same backing materials and support structure used for the target except without the ^{241}Am. This way we measured the background caused by the elastic scattered neutrons from the target backing. The contribution of neutron elastic scattering on the ^{241}Am material cannot be measured directly but can be estimated from the barium capture events. Therefore, the background total γ-ray energy spectrum

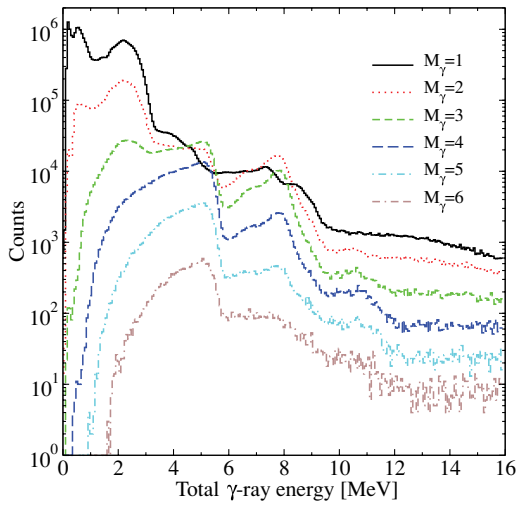

FIG. 3. (Color online) Total γ-ray energy E_γ^{total} spectra for cluster multiplicity $M_\gamma = 1$–6 for neutron energies 0.02–100 eV.

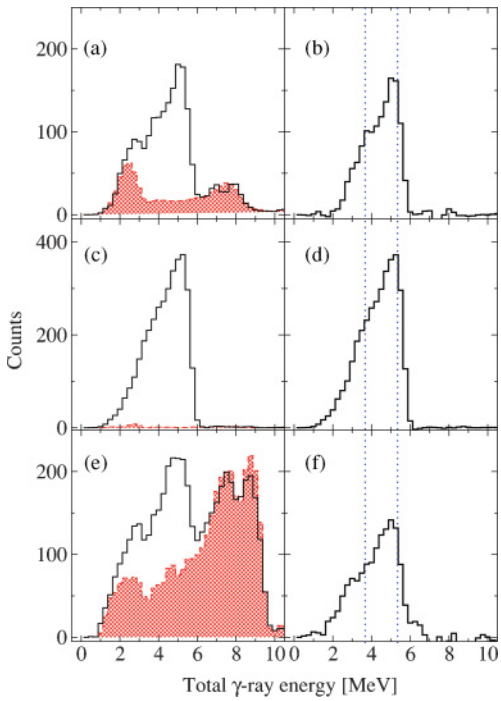

FIG. 4. (Color online) Total γ-ray spectra for data on ^{241}Am target (solid line) and normalized total γ-ray spectra on the blank target (stippled area) for cluster multiplicity $M_\gamma = 4$ and neutron energies (a) $E_n = 0.02516$–0.02542 eV, (c) $E_n = 0.3035$–0.3066 eV, and (e) $E_n = 1.025$–1.252 keV. Panels (b), (d), and (f) show the total γ-ray energy spectra obtained after the subtraction of the background spectra in panels (a), (c) and (e), respectively, and they represent ^{241}Am(n, γ) total γ-ray energy spectra for $M_\gamma = 4$. Dashed vertical lines show the region of E_γ^{total} used in the final analysis.

was normalized to the number of events above the ^{241}Am(n, γ) reaction Q value ($6.0 < E_\gamma^{\text{total}} < 7.9$ MeV) measured with the ^{241}Am target, to account for this background also. A detailed analysis of signal-to-noise ratio determined that the smallest uncertainties in the cross section determination are achieved if events with the cluster multiplicity $M_\gamma = 4$ and total γ-ray energy $3.75 < E_\gamma^{\text{total}} < 5.4$ MeV are used. The background subtraction procedure was performed for the total γ-ray energy spectra for all neutron energy bins. Figure 4 shows total γ-ray energy spectra for cluster multiplicity $M_\gamma = 4$. Panels (a), (c), and (e) show total γ-ray spectra for data on the ^{241}Am target (solid line) and normalized total γ-ray spectra on the blank target (stippled area) for cluster multiplicity $M_\gamma = 4$ and neutron energies (a) $E_n = 0.02516$–0.02542 eV, (c) $E_n = 0.3035$–0.3066 eV, and (e) $E_n = 1.025$–1.252 keV. Panels (b), (d), and (f) show the total γ-ray energy spectrum obtained after the subtraction of the spectra in panels (a), (c), and (e), respectively, and they represent ^{241}Am(n, γ) total γ-ray energy spectra for $M_\gamma = 4$. The background spectra in panels (a), (c), and (e) were normalized based on the number of counts in the total γ-ray energy region $6.0 < E_\gamma^{\text{total}} < 7.9$ MeV. For the final cross section data, only counts in the $3.75 < E_\gamma^{\text{total}} < 5.4$ MeV region of the subtracted spectra [shown in panels (b), (d), and (f) inside the region between the two dashed lines] were used for the cross section determination.

B. Efficiency of capture cascade detection

The cross section at the resonances is typically a few orders of magnitude higher than in between the resonances. The experimental count rate behaves the same way. On the other hand, the background is a rather smooth function of the neutron energy. Thus, taking two neutron energy bins, the first one on a resonance and the second one in the valley between resonances, the total γ-ray energy spectra in the two neutron energy bins will have similar contributions from the background but a few orders of magnitude different contribution from ^{241}Am(n, γ) capture. Subtracting these two spectra leads to a very effective background subtraction method. We cross-checked this method using different bins of neutron energy at the resonance and in the valleys and found no significant change in the γ-ray energy spectra.

The experimental spectra of total γ-ray energy at the 0.308 eV ($J^\pi = 2^-$) resonance and the valley at 0.4 eV are shown for the cluster γ-ray multiplicity $M_\gamma = 1$–5 in the left column of Fig. 5, where the solid line shows the spectra at the resonance and the stippled area shows the spectra in the valley. The shapes of both total γ-ray spectra are identical in the region above 6 MeV. The γ-ray spectrum in this region is mainly due to scattered neutrons that capture on Ba in the crystals. The spectrum in the valley is normalized here to the spectrum at the resonance to eliminate the scattered neutron contribution. By subtracting these two spectra for each γ-ray multiplicity, we obtain the total γ-ray energy spectrum for γ rays following neutron capture. The results are shown in the center column of Fig. 5. The third column of Fig. 5 shows the spectra of individual γ-ray energies obtained by gating on the total γ-ray energy $4.5 < E_\gamma^{\text{total}} < 5.5$ MeV. Together with the experimental spectra, the second and third columns of Figure 5 show the results of theoretical calculations of neutron capture cascades (dotted lines). The calculated spectra are in very good agreement with what is observed.

The emission of γ rays was simulated using the Monte Carlo statistical code DICEBOX; a detailed description of this code is given in Ref. [23]. DICEBOX uses information on all known energy levels, their spin, and decay modes up to some critical energy E_{crit}. Above E_{crit}, the level density and the photon strength function are described by various models. The models are entered as input parameter options in DICEBOX. The back-shifted Fermi gas model is used for the level density. The parametrizations are adapted from the RIPL-2 compilation [24] and Ref. [25]. A Monte Carlo simulation of the γ-ray cascades requires knowledge of partial radiation widths, and these are given by

$$\Gamma_{ab} = \sum_{X,L} y_{XL}^2 (E_a - E_b)^{2L+1} \frac{f_{XL}(E_a - E_b)}{\rho\left(E_a, J_a^{\pi_a}\right)}, \qquad (3)$$

where a and b indices denote the initial and final state, respectively; y_{XL} is a random variable with zero mean and unit variance, giving rise to Porter-Thomas distribution of partial γ widths; f_{XL} is the photon strength function for the given electromagnetic type and multipolarity XL; and $\rho(E_a, J_a^{\pi_a})$ is the spin-dependent nuclear level density. We used known

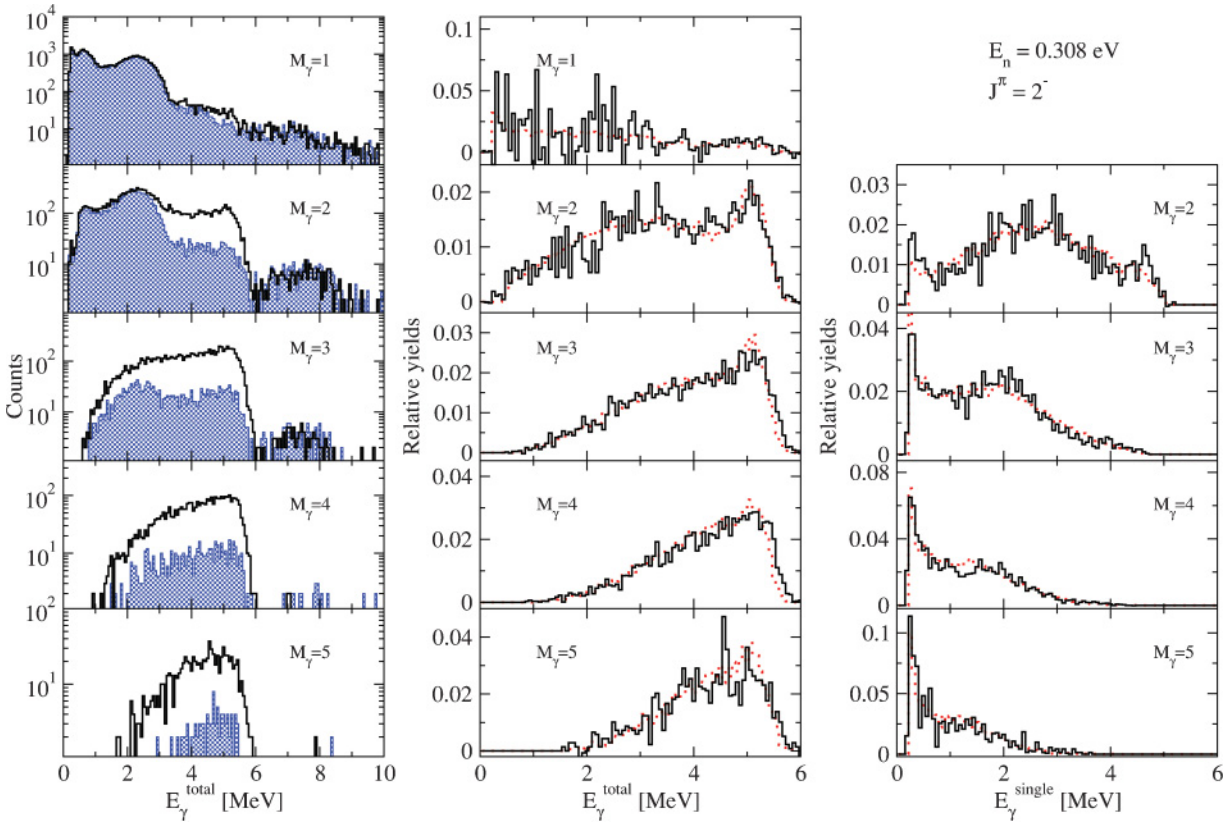

FIG. 5. (Color online) γ-ray energy spectra at $J^\pi = 2^-$, $E_n = 0.308$ eV resonance. Left column: total γ-ray energy spectrum at the resonance (solid line) and in the valley between the 0.3 and 0.5 eV resonances (stippled area) used for the background subtraction. Center column: total γ-ray energy spectrum after the subtraction of the background which was normalized in the region 6–7.9 MeV (solid line) compared with a DICEBOX-GEANT4 calculation (dotted line). Right column: measured individual γ-ray energy spectra obtained by gating on the total γ-ray energy in the region 4.5–5.5 MeV (solid line) compared with a DICEBOX-GEANT4 calculation (dotted line).

data on ^{241}Am energy levels and spins. The giant electric dipole resonance (GEDR) was modeled by the generalized Lorentzian model and was composed of two Lorentzians with the following parameters: the centroid $E_\gamma = 10.82$ MeV, the width $\Gamma = 2.44$ MeV, the strength $\sigma = 325.0$ mb for the first peak, and $E_\gamma = 13.83$ MeV, $\Gamma = 3.88$ MeV, and $\sigma = 384.0$ mb for the second peak. The $M1$ photon strength function was composed of two parts: the spin-flip giant magnetic dipole resonance and the scissors-mode resonance. The parameters of the spin-flip resonance were adapted from the RIPL-2 library [24], the centroid at $E_\gamma = 6.58$ MeV, the width $\Gamma = 4.0$ MeV, and the strength $\sigma = 4.0$ mb. The parameters for the scissors-mode resonance were estimated to be $E_\gamma = 2.5$ MeV, $\Gamma = 0.6$ MeV, and $\sigma = 0.8$ mb. Another very important feature of the DICEBOX code is its proper treatment of the internal electron conversion, which plays an important role in the decay of the odd-odd ^{242}Am compound nucleus because the level density is high. Each electromagnetic transition in the γ-ray cascades produced by the DICEBOX code carries a flag indicating whether the energy is radiated via photon or conversion electron. In generating the summed and singles γ-ray spectra, these flags are included in the analysis.

After the DICEBOX calculation, γ-ray cascades were run in the calibrated GEANT4 software replica of the DANCE array, to account for the detector response [18].

The resulting efficiency curve was constructed by taking the integrals of the E_γ^{total} spectra over the entire energy region for each multiplicity and is shown in Fig. 7(a) (solid line). Again, the DICEBOX-GEANT4 calculation is shown (dashed line) which is in excellent agreement with the experimental values.

The same procedure was carried out for the $E_n = 1.268$ eV resonance with a spin state $J^\pi = 3^-$ [see Figs. 6 and 7(b)]. The multiplicity distributions are identical for different spin states within the statistical errors. These results are important because they show that for the ^{241}Am target, spectra from the DANCE array cannot be used to distinguish between the spins of the resonances, contrary to the case of neutron capture on Mo and Sm isotopes [26,27]. We believe that this result can be attributed to the higher level density in ^{242}Am. The model calculations using DICEBOX-GEANT4 confirmed the experimental data.

The efficiency of capture cascade detection $\varepsilon_{n,\gamma}$ was determined to be 12.5(1)% for events with the total γ-ray energy $3.75 < E_\gamma^{\text{total}} < 5.4$ MeV and multiplicity $M_\gamma = 4$. The same value of $\varepsilon_{n,\gamma}$ was used for all neutron energies as

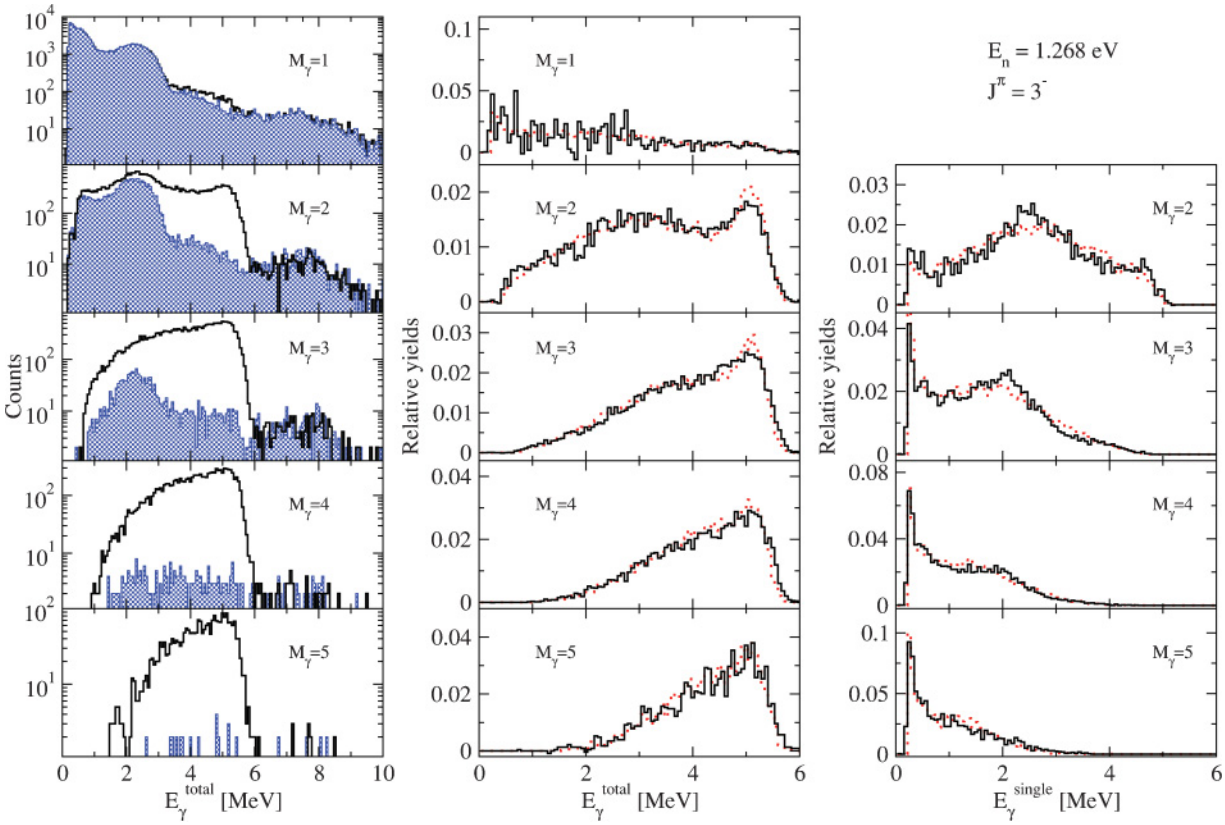

FIG. 6. (Color online) Same as Fig. 5, but for the $J^\pi = 3^-$, $E_n = 1.268$ eV resonance.

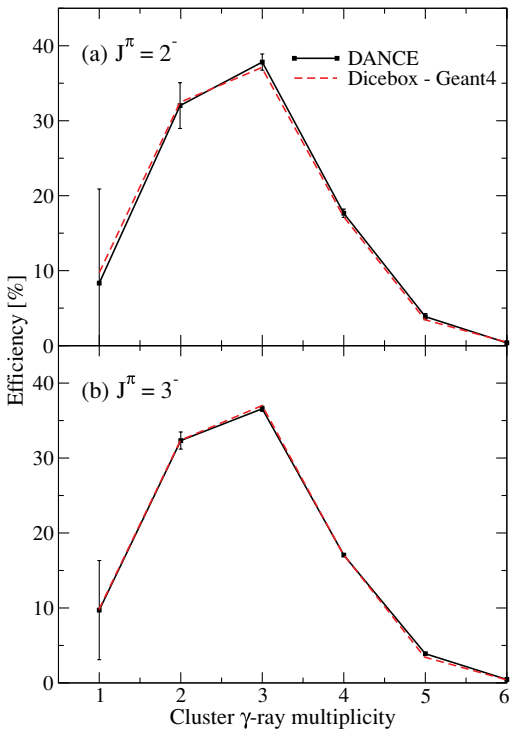

FIG. 7. (Color online) Experimental efficiency deduced from the yields for given cluster multiplicity (solid line) compared to DICEBOX-GEANT4 calculation (dashed line) at (a) the $J^\pi = 2^-$, $E_n = 0.308$ eV resonance and (b) the $J^\pi = 3^-$, $E_n = 1.268$ eV resonance.

mentioned above, as no evidence of spin-dependent efficiency was found.

C. Neutron flux determination

1. Neutron beam monitors

The incident neutron flux was measured with three neutron detectors located downstream of the DANCE array. The first neutron monitor consists of a ^{6}LiF target (of thickness 2 μm and size 3×4 cm^2) deposited on an 8-μm-thick Kapton foil and positioned in the center of the beampipe at a 45° angle, approximately 22.59 m from the neutron moderator. An n-type surface barrier Si detector was located perpendicular to the beam at a distance of 3 cm from the ^{6}Li foil. Tritons and α particles produced in the ^{6}Li(n,t)^{4}He reaction were measured.

The second monitor, positioned at 22.76 m from the moderator, was an ionization chamber filled with BF_3+Ar gas. The ^{10}B$(n, \alpha)^7$Li reaction products were measured.

The third neutron monitor was a ^{235}U fission chamber filled with P-10 gas. The sample of 1.3 mg/cm^2 (total mass ~50 mg with a sensitive diameter of 6.99 cm) of 93% enriched ^{235}U was located in the center of the chamber, 22.82 m from the moderator. Neutron-induced fission products were detected.

Signals from each neutron detector were shaped in fast shaping amplifiers to obtain similar signal wave forms from

each monitor. This approach simplified the signal processing in the online wave-form analysis. The shaped pulses were 2.85 μs long. Using 50-ns sampling in the Acqiris DC270 module allowed us to cover continuously the 14-ms window from the beam trigger. The signal from each monitor was saved to the disk if the leading edge was detected in the online analysis. The neutron monitor signals were reduced in the same manner as the signals from the BaF_2 crystals, i.e., 32 points sampled at 50 ns starting 250 ns before the leading edge of the peak and five sequential integrals of 250 ns intervals. In the off-line analysis, two integrals were calculated from the beam monitor signals. The integral of the first 1.6 μs of the signal I_1 was determined from the sum of the first 32 points of the signal. The integral I_2 of a signal tail that followed immediately after I_1 was determined as a sum of the five integrals saved by the front-end data acquisition system.

Evidence of pileup events was observed in the neutron flux monitors in the thermal neutron energy region. These pileup events were mainly caused by the fixed resolving time in the front-end data acquisition system and its peak-search routine, which did not allow for the detection of more than one pulse within a 2.8-μs blocking time. The maximum pileup correction reached 1.9% at 0.05 eV in the ^{6}Li monitor. For the BF_3 and ^{235}U monitors, the pileup correction was less than 0.5%. The integrals I_1 and I_2 were used to discriminate reaction products from the background and pileup events. In this manner, the efficiency of the detection of neutron-induced events in the beam monitors was dependent on the gate in the pulse height spectra. No attempt was made in this work to determine the absolute efficiency of the beam monitors. Instead, we calibrated the absolute neutron flux at the target position using standard Au targets, as will be described later in Sec. III C3. The gates on the pulse height spectra in the beam monitors were kept fixed when analyzing Au and ^{241}Am data.

The event rates detected by the neutron monitors were converted to neutron fluxes using known evaluated ENDF/B-VII cross sections. The ^{6}Li(n, t) cross section was determined from the ENDF/B-VII.0 evaluation for the total cross section and angular distribution, and the scattering angle was evaluated at 90° in the laboratory frame.

2. *Determination of the distance between the neutron moderator and the beam monitors*

The relative distances between the neutron beam monitors were measured. The precise determination of the distance between the monitors and the moderator was performed in the following manner. The neutron energy spectrum $N_{^{235}\mathrm{U}}(E)$ obtained in the ^{235}U monitor divided by the flux $\Phi_{\mathrm{BF_3}}(E)$ measured by the BF_3 monitor is directly proportional to the U(n, f) cross section, i.e., $\sigma(n, f) \propto N_{^{235}\mathrm{U}}(E)/\Phi_{\mathrm{BF_3}}(E)$. Both $N_{^{235}\mathrm{U}}(E)$ and $\Phi_{\mathrm{BF_3}}(E)$ are dependent on the flight-path distance; and using the R-matrix-based resonance-fitting code SAMMY [28], we fit the cross section for different flight-path lengths to obtain the best value. The flight-path length between the moderator and ^{235}U fission chamber was varied from 22.65 to 22.95 m in 1-cm increments. The best fit was obtained for 22.82 m.

3. *Determination of neutron flux at the target position using* ^{197}Au *targets*

The flight path has four sets of collimators outside of the bulk shield surrounding the neutron production target. The first three are large-aperture collimators designed primarily to reduce the off-center flux incident on the fourth. The fourth collimator defines the beam spot, which has minimal penumbra. This collimator is a double-tapered collimator 1 m in length composed of copper, polyethylene, and tungsten. The smallest aperture is 0.6 cm in diameter at 18.37–18.62 m from the moderator face. The neutron beam diverges with increasing distance from the last collimator in the flight path upstream of the DANCE target position. The neutron flux $\Phi_{\mathrm{BF_3}}$ measured in the BF_3 monitor is therefore not the same as the neutron flux Φ at the target position in the center of DANCE. This fact was confirmed with the image plate measurements taken at the beam entry and beam exit of the DANCE array and at the neutron monitor position. The beam spot at the BF_3 monitor has a diameter of ∼1.4 cm, whereas the beam spot at the entry to the DANCE ball is approximately 1 cm in diameter. The relation between the two fluxes is $\Phi = A\Phi_{\mathrm{BF_3}}$.

Additional measurements were performed to determine the value of A in order to obtain the neutron flux at the target position. Several targets of ^{197}Au in the shape of a disk were prepared by evaporation on a Mylar foil. The gold diameters were 2, 4, 7, 10, 15, and 20 mm, and the gold's thickness was approximately 0.5 μm. The exact thickness of the gold foil was determined using Rutherford backscattering spectrometry (RBS) on the 3-MV tandem Pelletron ion accelerator at the Ion Beam Materials Laboratory (IBML) at Los Alamos National Laboratory. The RBS measurements were performed with a 1.5-MeV H+ beam with a beam spot size of 1.5 × 1.5 mm^2. The backscattered protons from the gold were detected by a silicon surface barrier detector at a backward angle of 167° from the incident beam direction. A small beam current of ∼5 nA was used during the entire set of measurements to reduce beam heating effects on the Mylar substrate as well as to keep dead-time corrections low. The system was calibrated with a NIST Au film standard with a thickness of 442 nm. The conversion between thickness and areal density was done assuming a gold density of 5.91 × 10^{22} atoms/cm^3 for both the NIST standards and the gold targets.

Data on the ^{197}Au(n, γ) reaction were obtained using two ^{197}Au foils of different diameter (4 and 7 mm radius) before and after the ^{241}Am experiment. The analysis of this gold data was performed by gating on the 4.9-eV resonance, but without any multiplicity or total γ-ray energy requirements. For the cross section analysis, the flux measured by the BF_3 monitor $\Phi_{\mathrm{BF_3}}(E_n)$ was used. The background subtraction was carefully performed using data directly above the 4.9-eV resonance. The result was fitted with SAMMY where only a total normalization factor A was varied. A self-shielding correction was included in the analysis. The result obtained from the SAMMY fit was $A = 5.19$ for the 7-mm-diameter target and $A = 5.3$ for the 4-mm-diameter target. The final result of $A = 5.16(6)$ was then calculated using a linear interpolation for the 6.35-mm-diameter ^{241}Am sample.

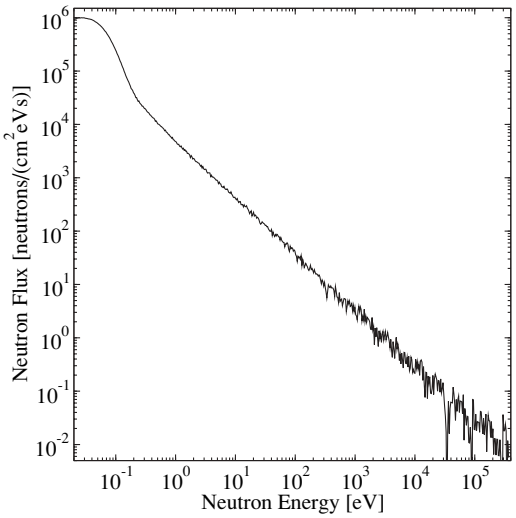

FIG. 8. Neutron flux measured with the BF_3 neutron monitor at the DANCE flight path. Average proton beam current was 100 μA. The dips at 35 and 88 keV are due to Al resonances in the shutter/production target assembly.

The normalized spectrum from the BF_3 neutron monitor was used in the cross section analysis for all neutron energy bins. The neutron flux measured with the BF_3 monitor is shown in Fig. 8.

IV. RESULTS AND DISCUSSION

All the ingredients needed to extract an absolute ^{241}Am(n,γ) cross section from the experimental data have now been presented. Here we summarize the quantities used for the final analysis:

(i) The yields of the neutron capture events were extracted for each neutron energy bin after the background subtraction.

(ii) The efficiency of the capture cascade detection $\varepsilon_{n,\gamma}$ after the cuts applied in the data analysis on cluster multiplicity $M_\gamma = 4$ and $3.75 < E_\gamma^{\text{total}} < 5.4$ MeV was determined to be $\varepsilon_{n,\gamma} = 0.125(1)$.

(iii) The neutron flux at target position was determined for each neutron energy bin using the flux spectrum from the BF_3 monitor Φ_{BF_3} corrected according to $\Phi = A\Phi_{BF_3}$, where $A = 5.16(6)$.

(iv) The mass of the target was 219(1) μg, and the illuminated area of the target was $S = 0.317$ cm^2.

The cross section was obtained in the region of neutron energy from 0.0253 eV to 320 keV. The result is shown in Fig. 9 compared with the ENDF/B-VII.0 [29], JEFF-3.1 [30], and JENDL-3.3 [31] evaluations.

A. Cross section at thermal energy

The cross section at $E_n = 0.0253$ eV was determined to be $\sigma_{\text{th}} = 665 \pm 33$ b. The relatively large uncertainty of 5% is caused in large part by inconsistency in the ^{6}Li and BF_3 neutron flux monitors that we observed at low energies ($E_n <$ 0.1 eV). The difference was probably caused by differences in the neutron scattering background in the different monitors; however, from the current data, we were not able to quantify it. Therefore, we have added 5% systematic error to the cross sections that we report up to 0.1 eV. Above $E_n = 0.1$ eV, the two neutron monitors give neutron fluxes that agree within 1%. The cross sections measured in this work in the region from 0.02 to 0.4 eV are shown in Fig. 10 together with the evaluated cross sections from the ENDF/B-VII.0 [29], JEFF-3.1 [30], and JENDL-3.3 [31] libraries. In the region around 0.1 eV, our results are most consistent with the JENDL-3.3 [31] evaluation. At thermal energy, we obtained a higher value than found in all three evaluations. The data on the thermal cross section are summarized in Table I. There is quite a spread in the experimental measurements. Our result agrees well with

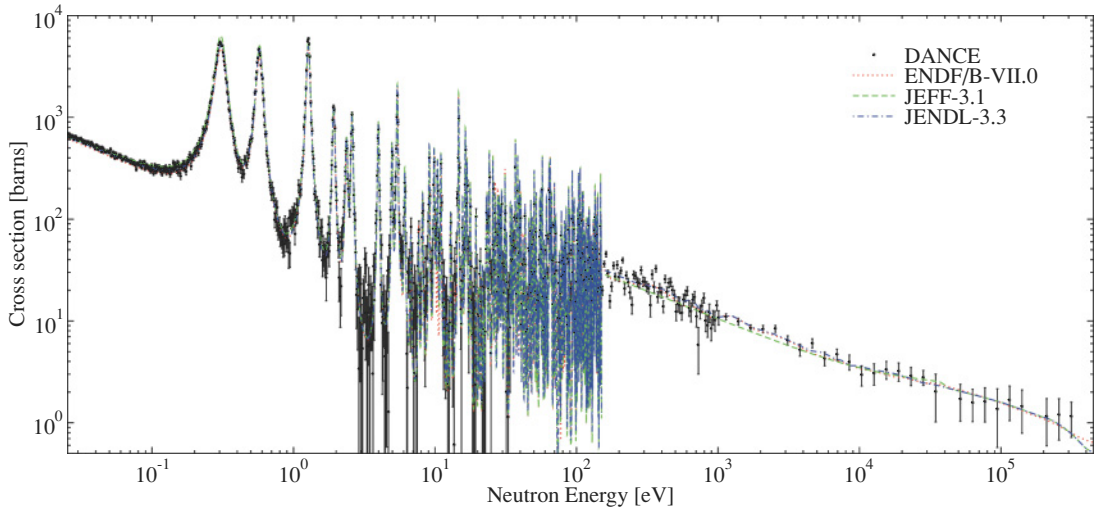

FIG. 9. (Color online) ^{241}Am(n,γ) cross sections measured with DANCE in the neutron energy region between thermal and 320 keV. The lines represent the ENDF/B-VII.0 [29], JEFF-3.1 [30], and JENDL-3.3 [31] evaluated cross sections.

TABLE I. Experimental and evaluated thermal neutron capture cross sections and resonance integrals RI above 0.5 eV for ^{241}Am.

Reference	Year	σ_{th} (b)	RI (b)
Experiment			
This work	2007	665 ± 33	1553 ± 7
Nakamura *et al.*[a] [2]	2007	690	
Fioni *et al.* [3]	2001	696 ± 48	
Maidana *et al.* [4]	2001	672 ± 10	
Shinohara *et al.* [5]	1997	854 ± 58	1808 ± 146
Wisshak *et al.* [12]	1982	625 ± 35	
Belanova *et al.* [6]	1976	622	
Adamchuk *et al.* [7]	1976	600	
Kalebin *et al.* [8]	1976	625 ± 20	
Weston *et al.* [13]	1976	582 ± 50	
Harbour *et al.* [10]	1973	612 ± 25	
Dovbenko *et al.* [9]	1971	654 ± 104	
Pomerance [11]	1955	625 ± 35	
Evaluation			
Mughabghab [33]	2006	585 ± 12	1425 ± 112
JEFF-3.1[b] [30]	2006	647 ± 32	1526.4
ENDF/B-VII.0[c] [29]	2006	620 ± 13	
JENDL-3.3 [31]	2002	639.4	1460

[a]Derived from $\sigma_{0,g} = 628 \pm 22$ b using branching ratio of 0.9±0.09 for the isomer state production.
[b]Based on Refs. [3,4,6,7].
[c]Based on Refs. [8–13].

the more recent measurements [2–4], which report larger cross section values than those measured in the 1970s and 1980s. The only evaluation that includes the recent measurements is the JEFF-3.1 evaluation.

B. Resonance region up to 12 eV

Figure 11 shows the cross section obtained in the region between thermal energy and ∼12 eV with the corresponding SAMMY fit [28] to the data. The resulting resonance parameters are given in Tables II and III. The SAMMY fit includes Doppler broadening, multiple scattering, self-shielding, and the moderator broadening function obtained in Ref. [26]. The initial resonance parameters were taken from ENDF/B-VII.0 evaluations. The Γ_n and Γ_γ widths and resonance energies E_0 were free parameters for the first six resonances. For other resonances, only the Γ_n was varied during the SAMMY fitting procedure. Table II compares the resonance parameters of the ENDF/B-VII.0 [29] and Mughabghab [33] evaluations to our results. In Table III, the JEFF-3.1 [30] and JENDL-3.3 [31] resonance parameters are contrasted to our results.

Values obtained for $2g\Gamma_n$ in this work for the first three resonances are significantly larger than the corresponding ones in the ENDF/B-VII.0 evaluation and Mughabghab evaluation. Our data seem to fall between the JENDL-3.3 and JEFF-3.1 evaluations for these resonances. Also, our results for the Γ_γ widths for these resonances seem to agree better with data evaluations of JENDL-3.3 and JEFF-3.1. Finally, the 10.5-eV resonance appears to be correctly given in the JENDL-3.3 and JEFF-3.1 evaluations, but it is dramatically underestimated in the ENDF/B-VII.0 evaluation.

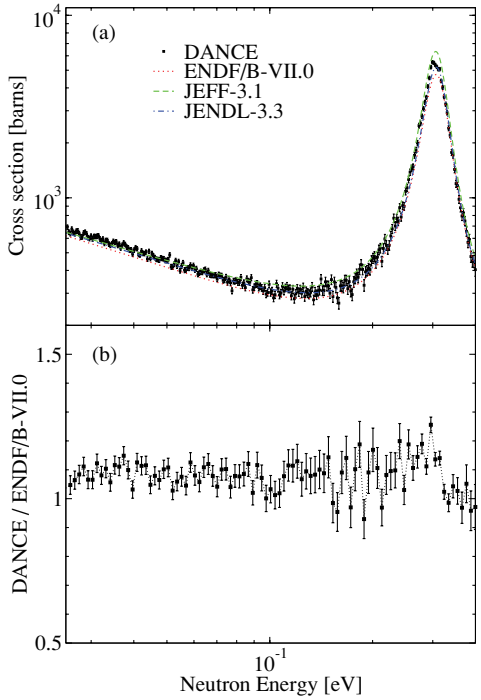

FIG. 10. (Color online) (a) ^{241}Am(n,γ) cross section measured in the low-energy region between 0.02 and 0.4 eV compared with evaluated cross sections. (b) Ratio of the ^{241}Am(n,γ) cross section measured with DANCE and the ENDF/B-VII.0 evaluated cross section (not all data points are shown for clarity).

The resonance integral

$$\mathrm{RI} = \int_{E_c}^{\infty} \frac{\sigma}{E} dE \tag{4}$$

was calculated from the experimental data above $E_c = 0.5$ eV. The value of 1553±7 b was obtained. In Table I the values of evaluated resonance integrals are shown together with our result.

C. Neutron energies between 12 eV and 320 keV

The data for energies above 12 eV are shown in Fig. 12, together with the JENDL-3.3, ENDF/B-VII.0, and JEFF-3.1 evaluated cross sections. Neutron capture cross sections at higher energies behave more smoothly (but often fluctuations persist) than those in the resonance region, since the resonances are strongly overlapped. In this energy region, averaged properties of the resonances can be defined, such as the averaged spacing of the s-wave resonances D_0, and the averaged widths for different reaction channels, such as $\langle\Gamma_n\rangle$ for neutron scattering, $\langle\Gamma_\gamma\rangle$ for radiative capture, and $\langle\Gamma_f\rangle$ for fission. These averaged properties of the resolved resonances are the key ingredients of the Hauser-Feshbach statistical theory, which predicts the averaged cross sections in the unresolved resonance region.

We performed calculations using the Hauser-Feshbach theory with a width-fluctuation correction based on the work

TABLE II. Resonance parameters for neutron resonances in the energy region between 0.3 and 12 eV. The results obtained from the SAMMY fit to our data are compared with existing values from ENDF/B-VII.0 [29] and Mughabghab [33] evaluations. No error bars are given for our results if that particular parameter was kept fixed during the SAMMY fit.

ENDF/B-VII.0			Mughabghab [33]			This work		
E_0 (eV)	Γ_γ (meV)	$2g\Gamma_n$ (meV)	E_0 (eV)	Γ_γ (meV)	$2g\Gamma_n$ (meV)	E_0 (eV)	Γ_γ (meV)	$2g\Gamma_n$ (meV)
0.308	46.9	0.056935	0.307(2)	46.8(3)	0.0560(5)	0.3051(2)	44.4(3)	0.0622(4)
0.576	47.3	0.0929	0.574(4)	47.2(3)	0.0923(2)	0.5724(3)	43.3(5)	0.1030(7)
1.276	47.9	0.322	1.268(4)	49.6(7)	0.320(8)	1.2718(4)	45.3(7)	0.347(4)
1.928	44.6	0.11133	1.930(5)	44.6(3)	0.113(2)	1.922(1)	41(2)	0.117(2)
2.372	44	0.071666	2.380(8)	42.7(3)	0.07(7)	2.363(2)	50(8)	0.078(3)
2.598	47.6	0.15	2.590(9)	46.6(6)	0.15(2)	2.599(2)	48(3)	0.147(4)
3.973	44.5	0.20966	3.97(1)	44.5(3)	0.22(6)	3.973	44.5	0.208(8)
4.968	43.8	0.17733	4.97(1)	43.8(4)	0.175(4)	4.968	43.8	0.178(7)
5.415	44.2	0.766	5.42(1)	44.2(1)	0.78(2)	5.415	44.2	0.74(2)
5.8	44.2	0.002	–	–	–	5.8	44.2	0.0020(2)
6.117	43.8	0.12366	6.12(1)	43.8(7)	0.127(2)	6.117	43.8	0.127(9)
6.745	44.2	0.032857	6.74(1)	–	0.030(2)	6.745	44.2	0.033(3)
7.659	44.2	0.04557	7.66(1)	–	0.039(2)	7.659	44.2	0.048(5)
8.173	42.7	0.107	8.17(1)	42.7±1.2	0.107(3)	8.173	42.7	0.105(7)
9.113	44.2	0.37733	9.12(2)	44.2(6)	0.379(8)	9.113	44.2	0.364(24)
9.851	43.9	0.39766	9.85(2)	43.9(6)	0.40(1)	9.851	43.9	0.40(2)
10.116	44.2	0.0255	10.12(2)	–	0.026(1)	10.116	44.2	0.027(3)
10.403	42.4	0.148767	10.43(2)	42.4(8)	0.33(1)	10.404(6)	45(4)	0.35(2)
10.997	46.5	0.40333	10.98(2)	46.5(8)	0.40(2)	10.997	46.5	0.41(3)
11.583	44.2	0.021333	11.58(2)	–	0.016(1)	11.583	44.2	0.022(2)

of Moldauer [34], and with the refined channel degree-of-freedom systematics of Ernebjerg and Herman [35]. Although the fission cross sections for ^{241}Am in the neutron energy region of the present analysis are almost negligible, we do include the fission channel as a competing channel to that of neutron and γ-ray emission processes.

TABLE III. Resonance parameters for neutron resonances in the energy region between 0.3 and 12 eV. The results obtained from the SAMMY fit to our data are compared with existing values from JEFF-3.1 [30] and JENDL-3.3 [31] evaluations.

JENDL-3.3 [31]			JEFF-3.1 [30]			This work		
E_0 (eV)	Γ_γ (meV)	$2g\Gamma_n$ (meV)	E_0 (eV)	Γ_γ (meV)	$2g\Gamma_n$ (meV)	E_0 (eV)	Γ_γ (meV)	$2g\Gamma_n$ (meV)
0.308	44.680	0.060	0.307	43.528	0.072	0.3051(2)	44.4(3)	0.0622(4)
0.576	44.138	0.107	0.576	40.671	0.110	0.5724(3)	43.3(5)	0.1030(7)
1.272	47.000	0.304	1.273	48.436	0.339	1.2718(4)	45.3(7)	0.347(4)
1.924	45.000	0.115	1.923	48.993	0.122	1.922(1)	41(2)	0.117(2)
2.367	44.000	0.073	2.372	42.400	0.072	2.363(2)	50(8)	0.078(3)
2.591	47.000	0.145	2.597	46.100	0.153	2.599(2)	48(3)	0.147(4)
3.973	47.000	0.206	3.977	44.100	0.214	3.973	44.5	0.208(8)
4.968	44.000	0.171	4.966	43.300	0.178	4.968	43.8	0.178(7)
5.415	45.000	0.749	5.409	43.600	0.767	5.415	44.2	0.74(2)
5.800	58.000	0.005	5.800	58.000	0.005	5.8	44.2	0.0020(2)
6.117	49.000	0.125	6.115	43.400	0.131	6.117	43.8	0.127(9)
6.745	44.000	0.033	6.750	45.000	0.029	6.745	44.2	0.033(3)
7.659	44.000	0.037	7.669	45.000	0.038	7.659	44.2	0.048(5)
8.173	50.000	0.111	8.185	42.600	0.108	8.173	42.7	0.105(7)
9.113	49.000	0.385	9.125	44.000	0.389	9.113	44.2	0.364(24)
9.851	47.000	0.396	9.865	43.200	0.412	9.851	43.9	0.40(2)
10.116	61.000	0.028	10.130	45.000	0.026	10.116	44.2	0.027(3)
10.403	49.000	0.324	10.417	42.400	0.332	10.404(6)	45(4)	0.35(2)
10.997	51.000	0.404	11.013	46.600	0.410	10.997	46.5	0.41(3)
11.583	44.000	0.021	11.620	45.000	0.017	11.583	44.2	0.022(2)

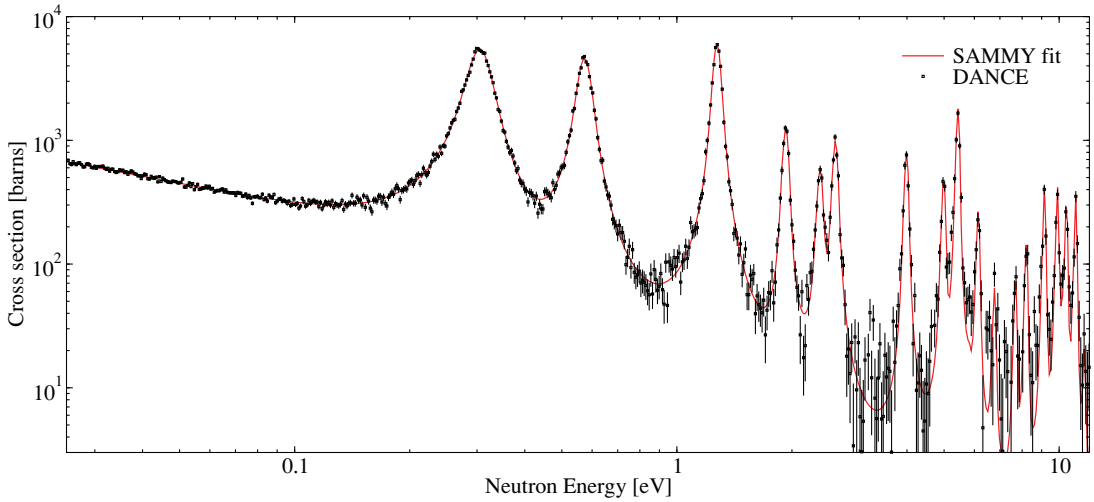

FIG. 11. (Color online) ^{241}Am(n,γ) cross section measured with DANCE in the neutron energy region between thermal and 12 eV. The solid line shows the SAMMY fit to the measured data.

The neutron width $\langle\Gamma_n\rangle$ can be related to the neutron transmission coefficients which are calculated with the coupled-channels theory. Talou *et al.* [36] obtained the coupled-channels optical potential for ^{241}Am that agrees well with the experimental total cross section data. Five ground-state rotational band levels, $5/2^-7/2^-9/2^-11/2^-13/2^-$, are included in these coupled-channels calculations. We reduced the imaginary potential depth slightly to obtain improved agreement with the evaluated s-wave neutron strength function. The calculated neutron strength function of $S_0 = 0.91 \times 10^{-4}$ which was obtained agrees well with the evaluated value of $S_0 = (0.90 \pm 0.09) \times 10^{-4}$ [33].

Capture cross sections in the keV energy range are sensitive to the γ-ray strength function $\langle\Gamma_\gamma\rangle/D_0$ used to renormalize the γ-ray transmission coefficients. The calculated capture cross section becomes insensitive to the level density of ^{242}Am when the γ-ray transmission coefficients are renormalized to a known $\langle\Gamma_\gamma\rangle/D_0$ value. For these calculations, we use level densities that are obtained from the systematic work of Kawano, Chiba, and Koura [37]. The averaged s-wave resonance spacing D_0 and the averaged γ-ray width $\langle\Gamma_\gamma\rangle$ are taken to be 0.55 and 0.045 eV, respectively [33]. For the neutron inelastic scattering, uncoupled discrete levels are included up to the 732-keV $5/2^-$ level, and the level density formula is used above that energy. In Fig. 13, the calculated capture cross sections, shown by the solid curve, are compared with the DANCE data and those of two other experiments [14,15]. The calculation is not adjusted to the experimental data, but it does agree fairly well with the experiments.

Although the calculated cross sections reproduce the DANCE data well, we performed a least-squares fit by adjusting the $\langle\Gamma_\gamma\rangle/D_0$ value. The best-fit values obtained vary depending on which data points are included in the least-squares fitting. For example, if we include the DANCE data above 10 keV, the best $\langle\Gamma_\gamma\rangle$ value becomes slightly less than 0.045 eV. If the data below 10 keV are included, $\langle\Gamma_\gamma\rangle$ becomes slightly higher than 0.045 eV upon χ^2 minimization. Therefore the $\langle\Gamma_\gamma\rangle = 0.045$ eV as stated in Mughabghab [33] seems to do reasonably well in reproducing the experimental data over the energy range of interest. This confirms the fact that our current analysis is consistent in both the resolved and unresolved resonance regions.

Calculated and measured neutron capture rates on ^{241}Am inside different critical assembly spectra were reported in

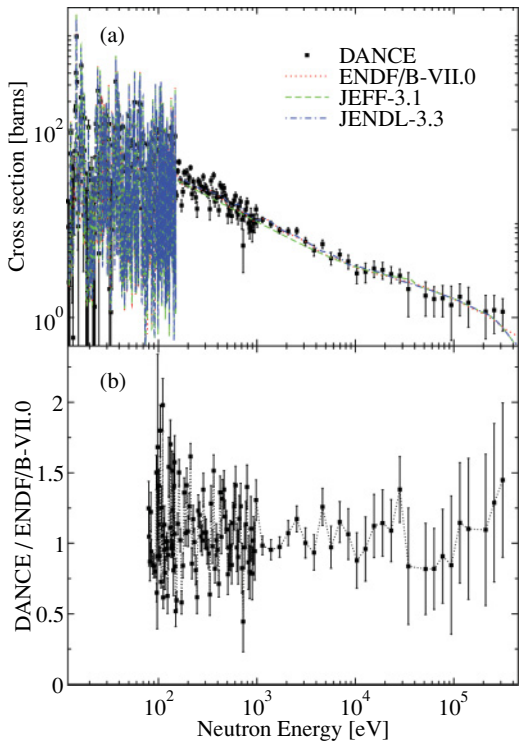

FIG. 12. (Color online) (a) ^{241}Am(n,γ) cross sections measured with DANCE in the high neutron energy region above 20 eV compared with data evaluations. (b) Ratio of the ^{241}Am(n,γ) cross section measured with DANCE and the ENDF/B-VII.0 evaluated cross section (not all data points are shown for neutron energy below 150 eV).

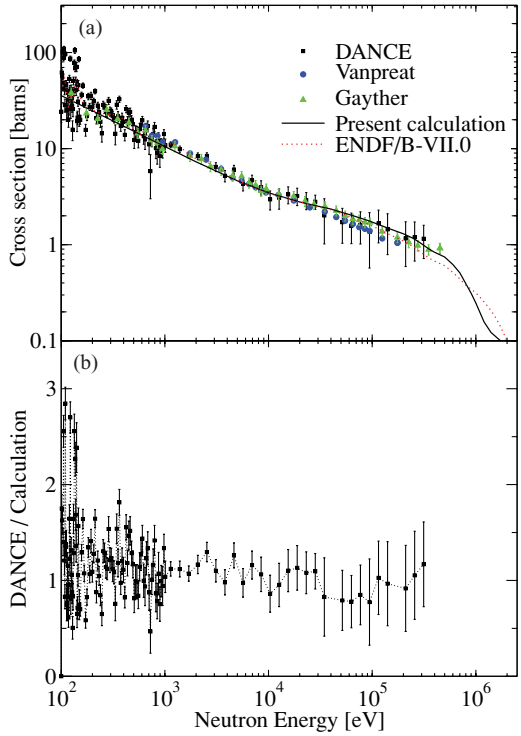

FIG. 13. (Color online) (a) Comparison of the calculated capture cross sections with the DANCE experimental data, Gaither and Thomas [14], and Vanpraet *et al*. [15]. The solid curve is the result of statistical model calculation with $\langle\Gamma_\gamma\rangle = 0.045$ eV. (b) Ratio of the ^{241}Am(n,γ) cross section measured with DANCE and the present calculation (not all data points are shown for neutron energy below 150 eV).

Ref. [29] as an integral validation test of the ENDF/B-VII.0 data. The agreement between the calculated and measured values is in general good. However, for Jezebel (a solid plutonium sphere, which has the hardest neutron spectrum), the MCNP radiation transport simulation using the capture cross section in ENDF/B-VII.0 underestimated the measurement by about 6%, as seen in Fig. 108 of Ref. [29]. We have assessed how the new calculated capture cross section would perform in this same validation test. We simply estimated this value by calculating an averaged capture rate over the Jezebel neutron spectrum and found that our new capture data may give about a 5% higher capture rate than that obtained using the ENDF/B-VII.0 capture cross section, which is consistent with the experimental integral value. To perform this comparison in detail, MCNP Monte Carlo simulations are needed including all other critical systems to make sure that our capture cross section does not adversely change the integral values for other softer neutron spectra (which agreed well using the previous ENDF/B-VII.0 data); this work is in progress.

V. SUMMARY

The ^{241}Am(n,γ) cross section was measured for neutron energies between 0.02 eV and 320 keV. The uncertainties include all known systematic and statistical errors. Our neutron flux determination is referenced to the 4.9-eV resonance in ^{197}Au. The uncertainty of this normalization is negligible compared to our statistical uncertainties. The thermal neutron capture cross section was determined to be 665±33 b. Resonance parameters for $E_n < 12$ eV were obtained using a SAMMY fit to measured cross sections and compared with existing evaluations. The resonance integral above 0.5 eV was determined to be 1553±7 b. Γ_n neutron widths for first three resonances are systematically larger than the ENDF/B-VII.0 values by 5–15% and agree better with the JEFF-3.1 and JENDL-3.3 evaluations. Cross sections in the resolved and unresolved energy region above 12 eV were calculated using the Hauser-Feshbach theory with the width-fluctuation correction by Moldauer. The calculated results agree well with the measured data, and the extracted averaged resonance parameters in the unresolved resonance region are consistent with those for the resolved resonances.

ACKNOWLEDGMENTS

We would like to thank L. Leal of Oak Ridge National Laboratory, for his guidance and help in using the SAMMY code and M. Krtička and F. Bečvář of Charles University, Prague, for providing us with their code DICEBOX. This work benefited from the use of the LANSCE accelerator facility. Work was performed under the auspices of the U.S. Department of Energy at Los Alamos National Laboratory by the Los Alamos National Security, LLC under Contract No. DE-AC52-06NA25396 and at Lawrence Livermore National Laboratory by the Lawrence Livermore National Security, LLC under Contract No. DE-AC52-07NA27344.

APPENDIX: DEAD-TIME CORRECTION

The data acquisition of DANCE can be run in two modes. One of them, the so-called segmented mode, includes a fixed dead time of 3.5 μs after a trigger for every event (see Ref. [21] for more details on this DAQ mode). A dead-time correction needs to be calculated to account for the lost events during the dead time. We followed the derivation given in Refs. [38–40]. Details of the calculations are described in the following.

Events will be lost in channel n when channel n is dead. Events will also be lost if two or more events fall in the same channel if this channel is alive, since only one event will be recorded. Let d_n be the probability that channel n is dead, and $P_n(x)$ be the probability of receiving x true pulses per beam burst in channel n. Then the probability of losing k events is

$$d_n P_n(k) + (1 - d_n) P_n(k+1), \tag{A1}$$

and the average number of lost events in channel n per beam burst is

$$L_n = \sum_{k=1}^{\infty} k\,[(1-d_n)P_n(k+1) + d_n P_n(k)]\,. \tag{A2}$$

C_n, the average true count rate in the channel n, can be written as $\sum_{k=1}^{\infty} k P_n(k)$. C'_n, the observed count rate in the channel n, is given by $C_n - L_n$ which using the Poisson distribution for

P_n becomes

$$C'_n = (1 - d_n)[1 - \exp(-C_n)]. \quad \text{(A3)}$$

The probability that channel n is dead only depends on those channels preceding channel n. It is therefore given by the sum of the product of the probability that a particular channel receives at least one event and the probability that this channel will not be dead, over all those channels m which could make channel n dead. Therefore,

$$d_n = \sum_m [1 - P_m(0)](1 - d_m)$$

$$= \sum_m [1 - \exp(-C_m)](1 - d_m), \quad \text{(A4)}$$

which, using Eq. (A3), can be rewritten as

$$d_n = \sum_m C'_m. \quad \text{(A5)}$$

Finally, the true count rate in the channel n, C_n, can be found from Eqs. (A3) and (A5):

$$C_n = -\ln\left(1 - \frac{C'}{1 - \sum_m C'_m}\right). \quad \text{(A6)}$$

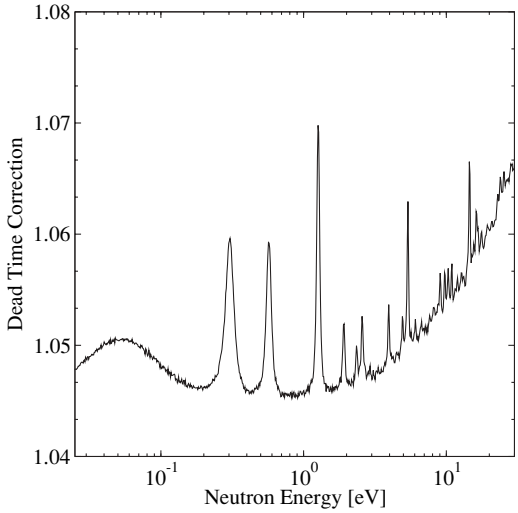

FIG. 14. Calculated dead-time correction to the measured data on ^{241}Am in segmented mode.

The neutron-energy-dependent dead-time correction applied to the segmented mode experimental data is shown in Fig. 14. The correction does not exceed 5% for neutron energies below 36 eV, where it was used for the cross section analysis.

[1] G. Aliberti, G. Palmiotti, M. Salvatores, T. K. Kim, T. A. Taiwo, M. Anitescu, I. Kodeli, E. Sartori, J. C. Bosq, and J. Tommasi, Ann. Nucl. Energy **33**, 700 (2006).

[2] S. Nakamura, M. Ohta, H. Harada, T. Fujii, and H. Yamana, J. Nucl. Sci. Technol. **44**, No. 12, 1500 (2007).

[3] G. Fioni, M. Cribier, F. Marie, M. Aubert, S. Ayrault *et al.*, Nucl. Phys. **A693**, 546 (2001).

[4] N. L. Maidana, M. S. Dias, and M. F. Koskinas, Radiochim. Acta **89**, 419 (2001).

[5] N. Shinohara, Y. Hatsukawa, K. Hata, and N. Kohno, J. Nucl. Sci. Technol. **34**, 613 (1997).

[6] T. Belanova *et al.*, EXFOR 40305.003 (1976).

[7] J. Adamchuk *et al.*, Nucl. Sci. Eng. **61**, 356 (1976).

[8] S. Kalebin *et al.*, Atomic Energy **40**, 373 (1976).

[9] A. Dovbenko *et al.*, Los Alamos National Laboratory Rep. LA-TR-71-74, 1971.

[10] R. Harbour *et al.*, Nucl. Sci. Eng. **50**, 364 (1973).

[11] H. Pomerance, Oak Ridge National Laboratory Rep. ORNL-1879, 1955, p. 50.

[12] K. Wisshak *et al.*, Nucl. Sci. Eng. **81**, 396 (1982).

[13] L. Weston *et al.*, Nucl. Sci. Eng. **61**, 356 (1976).

[14] D. B. Gayther and B. W. Thomas, in Proceedings of the 4th All Union Conference on Neutron Physics, Kiev, U.S.S.R., 18–22 Apr. 1977, Vol. 3, p. 3.

[15] G. Vanpraet, E. Cornelis, S. Raman, and G. Rohr, in Proceedings of the International Conference on Nuclear Data for Basic and Applied Science, Santa Fe, New Mexico, 13–17 May, 1985, p. 493; Radiat. Eff. **93**, 157 (1986).

[16] M. Heil, R. Reifarth, M. M. Fowler, R. C. Haight, F. Kaeppeler, R. S. Rundberg, E. H. Seabury, J. L. Ullmann, and K. Wisshak, Nucl. Instrum. Methods Phys. Res. A **459**, 229 (2001).

[17] P. W. Lisowski, C. D. Bowman, G. J. Russell, and S. A. Wender, Nucl. Sci. Eng. **106**, 208 (1990).

[18] M. Jandel, T. A. Bredeweg, A. Couture, M. M. Fowler, E. M. Bond, M. B. Chadwick, R. R. C. Clement, E.-I. Esch, J. M. O'Donnell, R. Reifarth, R. S. Rundberg, J. L. Ullmann, D. J. Vieira, J. B. Wilhelmy, J. M. Wouters, R. A. Macri, C. Y. Wu, and J. A. Becker, Nucl. Instrum. Methods Phys. Res. B **261**, 1117 (2007).

[19] M. R. Farukhi and C. F. Swinehart, IEEE Trans. Nucl. Sci. **18**, 200 (1971).

[20] M. Laval *et al.*, Nucl. Instrum. Methods **206**, 169 (1983).

[21] J. M. Wouters *et al.*, IEEE Trans. Nucl. Sci. **53**, 880 (2006).

[22] https://midas.psi.ch.

[23] F. Bečvář, Nucl. Instrum. Methods Phys. Res. A **417**, 434 (1998).

[24] http://www-nds.iaea.org/RIPL-2.

[25] T. Von Egidy, H. H. Schmidt, and A. N. Behkami, Nucl. Phys. **A481**, 189 (1988).

[26] P. E. Koehler *et al.*, Phys. Rev. C **76**, 025804 (2007).

[27] S. A. Sheets, U. Agvaanluvsan, J. A. Becker, F. Bečvář, T. A. Bredeweg, R. C. Haight, M. Krtička, M. Jandel, G. E. Mitchell, J. M. O'Donnell, W. E. Parker, R. Reifarth, R. S. Rundberg, E. I. Sharapov, I. Tomandl, J. L. Ullmann, D. J. Vieira, J. M. Wouters, J. B. Wilhelmy, and C. Y. Wu, Phys. Rev. C **76**, 064317 (2007).

[28] N. M. Larson, Oak Ridge National Laboratory Rep. ORNL/TM-9179/R7, 2006.

[29] M. A. Chadwick, P. Oblozinsky, M. Herman *et al.*, Nucl. Data Sheets **107**, 2931 (2006).

[30] A. Koning *et al.*, The JEFF-3.1 Nuclear Data Library, JEFF Report 21, 2006.

[31] K. Shibata *et al.*, J. Nucl. Sci. Technol. **39**, 1125 (2002).

[32] R. Reifarth *et al*., Nucl. Instrum. Methods Phys. Res. A **531**, 530 (2004).
[33] S. F. Mughabghab, *Atlas of Neutron Resonances, Resonance Parameters and Thermal Cross Sections Z = 1–100*, 5th ed. (Elsevier, New York, 2006).
[34] P. A. Moldauer, Nucl. Phys. **A344**, 185 (1980).
[35] M. Ernebjerg and M. Herman, AIP Conf. Proc. **769**, 1233 (2005).
[36] P. Talou, T. Kawano, P. G. Young, M. B. Chadwick, and R. E. MacFarlane, Nucl. Sci. Eng. **155**, 84 (2007).
[37] T. Kawano, S. Chiba, and H. Koura, J. Nucl. Sci. Technol. **43**, 1 (2006).
[38] C. D. Bowman and R. L. Bramblett, Lawrence Livermore National Laboratory Rep. LINAC-21, Feb. 1962.
[39] P. B. Coates, Rev. Sci. Instrum. **63**, 2084 (1992).
[40] M. S. Moore, Nucl. Instrum. Methods **169**, 245 (1980).